FAST DETECTION OF CONVERGENCE AREAS IN DIGITAL BREAST TOMOSYNTHESIS

G. Palma[†‡], *S. Muller*[†]

[†] GE Healthcare Europe
283, rue de la Minière, 78530 Buc, France

I. Bloch[‡], *R. Iordache*[†]

[‡] Télécom ParisTech (ENST)
CNRS UMR 5141
46, rue Barrault, 75013 Paris, France

ABSTRACT

In this paper we propose a fast method to detect spiculated lesions and architectural distortions in Digital Breast Tomosynthesis datasets. This approach relies on an a contrario modeling of the problem. First, an indicator corresponding to the convergence of structures is defined, then the a contrario framework is used to set a threshold on it in order to detect zones where its value is unlikely. We propose, as a main contribution of this paper, a fast algorithm to implement this method, which significantly reduces its computational cost.

The method was evaluated on 38 breasts (10 containing a lesion), and a sensitivity of 0.8 at 1.68 false positive per breast was obtained.

***Index Terms*—** Breast, Digital Breast Tomosynthesis CAD, spiculated masses, a contrario detection

1. INTRODUCTION

Mammography is the most favorable modality for the early detection of breast cancer. Because mammograms are projection images, they suffer from the superimposition of tissues, which may produce false alarms or hide lesions. Digital Breast Tomosynthesis (DBT), which is a new 3D imaging technique, has the potential to overcome these limitations. Unfortunately, the amount of data is greatly increased in comparison to regular mammograms. In this context it makes sense to provide the radiologist with a CAD system in order to help him to detect cancers, and thus to increase his sensitivity. Stellate patterns are common signs of presence of cancer [1]. Such shapes are usually detected using a convergence criterion. In [1] and [2], two similar measures based on two nested circles are proposed to process 2D mammograms and DBT slices, respectively.

The a contrario framework, which was originally designed to detect alignments of points [3], is a suitable approach to detect geometrical shapes in an image. This generic concept relies on the statistical definition of a naive model, which corresponds to the regular content of an image, and on the introduction of an event that is unlikely to appear in this modeling. This event is usually defined as a discriminant measure with respect to the structure we are looking for, and a threshold on this measure such that the number of occurrences of this event in the naive model is low. The approach was also applied to the modeling of the human detection task in complex background images [4] as well as the detection of convergence areas [2].

In this paper we propose to use an a contrario modeling for the detection of convergence areas. First, we describe the method introduced in [2], then we propose, as an original contribution, a fast implementation of this approach and discuss its complexity. Finally, we conclude on the performance of the detection scheme.

This work was realized under CIFRE convention 20061165 (GE Healthcate/Télécom ParisTech).

2. A CONTRARIO DETECTION OF CONVERGENCE AREAS

In order to detect convergence areas in DBT datasets, we proposed in [2] an a contrario modeling of the problem.

First, each slice of the volume is considered as a map of orientations defined on the image domain Ω and corresponding to the orientations of structures represented by the different pixels. In the naive model, which corresponds to a normal breast without lesion, these orientations are considered as independently and uniformly distributed angles. For real data, they are computed from vectors orthogonal to non correlated gradients in order to comply with the independence assumption [2]. Then, two random variables are defined on these orientation maps. These variables are defined for all the pixels of the maps, and rely on the definition of two nested circles as illustrated in Figure 1.

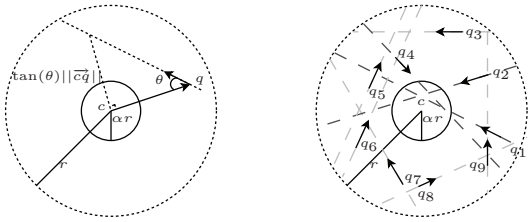

(a) (b)

Fig. 1. (a) Nested circles used for the computation of $K_{c,r,q}$ which is here equal to 0. (b) Computation of $Z_{c,r}$: the arrows on the dark dashed lines (passing through q_1, q_2 and q_4) converge while others do not.

These circles define the region of convergence for a spiculated lesion. The hole in the ring corresponds to the center of convergence, while the ring is the location where spicules should be found. Such a configuration can be expressed using three parameters: the center c of the circles, the radius r of the largest circle and a constant $\alpha \in]0, 1[$ such that αr is the radius of the smaller circle. The first random variable allows deciding whether a structure passing through a given pixel $q \in \Omega$ is converging according to the configuration of the two

circles:

$$K_{c,q,r} = \begin{cases} 1 \ \textit{if} (\alpha r < ||\overrightarrow{cq}|| < r) \wedge (\tan(\theta)||\overrightarrow{cq}|| \leq \alpha r) \\ 0 \ \textit{otherwise}. \end{cases}$$

where θ corresponds to the angle between $\overrightarrow{cq}$ and the orientation at point q.

The second random variable enables to count the number of points converging towards the center of the circles for the same configuration (c, r, α) and is defined as:

$$Z_{c,r} = \sum_{q \in \Omega} K_{c,q,r} \tag{1}$$

Using the statistics of the orientation map given by the naive model, we can derive the probability for $K_{c,q,r}$ to be equal to one, and thus the probability for $Z_{c,r}$ to be equal to a given integer [2]. This last probability is useful in order to detect convergence areas in real DBT slices. This is done using the definition of an ϵ-meaningful event [3]:

Definition 2.1. An event is ϵ-meaningful if the expectation of the number of its occurrences in the image is less than ϵ.

In our case, the considered event is $Z_{c,r} \geq \lambda_r$, with λ_r a threshold depending on r, ϵ and the total number M of couples (c, r) to consider:

$$\lambda_r = \min \left\{ \lambda \in \mathbb{N} / P[Z_{c,r} \geq \lambda] \leq \frac{\epsilon}{M} \right\}$$

In order to catch lesions of different sizes, we consider this event for each center c of the orientation map, and for radii ranging between $R_{\min}$ and $R_{\max}$ corresponding to possible lesion sizes. The thresholds λ_r are set such that the event is ϵ-meaningful according to Definition 2.1 [2]. These thresholds, which are deduced from the statistical definition of the content of an image, are used on the measures $Z_{c,r}$ computed on orientation maps extracted from real DBT slices. As mentioned earlier, these maps are deduced from non-correlated gradient. This point really matters since introducing new correlation would invalidate the thresholds λ_r, leading to an over-detection of convergence patterns. Let us also mention that if the naive model holds perfectly for real DBT slices, which means statistics about orientations are correct, the parameter ϵ used to compute the λ_r corresponds to the number of false alarms of the approach. Unfortunately, as it will be shown in Section 5, it is not the case, and a false positive reduction step is required.

3. FAST IMPLEMENTATION

A straightforward implementation of Equation 1 for a given range of radii may be rather inefficient and practically unusable when we may want to consider large structures. Nonetheless, we can remark that for a given center point c, if we consider two successive radii $r-1$ and r, some points q in Ω have the same convergence or non convergence property. Conversely, there exists a set of points that are converging for r while not for $r-1$. We consider the cardinality, denoted as $|.|$, of this set:

$$\delta_{c,r} = |\{q \in \Omega / (K_{c,q,r} = 1) \wedge (K_{c,q,r-1} = 0)\}| \tag{2}$$

Similarly, we can define the set of points that are converging for $r-1$, while not converging for r, and its cardinality:

$$\psi_{c,r} = |\{q \in \Omega / (K_{c,q,r} = 0) \wedge (K_{c,q,r-1} = 1)\}| \tag{3}$$

For the sake of clarity, let us introduce the following notation: $\forall b \in \{0,1\}\ C_r^b = \{q \in \Omega / K_{c,q,r} = b\}$, which enables to rewrite Equations 2 and 3 as follows:

$$\delta_{c,r} = |C_r^1 \cap C_{r-1}^0| \tag{4}$$

and

$$\psi_{c,r} = |C_r^0 \cap C_{r-1}^1| \tag{5}$$

These two quantities enable to decompose $Z_{c,r}$ as follows:

Theorem 3.1. $Z_{c,r} = \sum_{k=0}^{r} \delta_{c,k} - \sum_{k=0}^{r} \psi_{c,k}$

Proof. Let us prove the theorem by induction:
Initialization: Obviously, we have $Z_{c,0} = 0 - 0 = \delta_{c,0} - \psi_{c,0}$ since for any $(c, q) \in \Omega^2$ and $r \leq 0$, we have $K_{c,q,r} = 0$.
Induction: Let us assume that Theorem 3.1 holds for a given r. We can write:

$$\begin{aligned} Z_{c,r+1} &= \sum_{q \in \Omega} K_{c,q,r+1} \\ &= |C_{r+1}^1| \\ &= |C_{r+1}^1 \cap C_r^1| + |C_{r+1}^1 \cap C_r^0| \\ &= |C_{r+1}^1 \cap C_r^1| + \delta_{c,r+1} \text{ (c.f. Equation 4)} \\ &= |C_r^1| - |C_{r+1}^0 \cap C_r^1| + \delta_{c,r+1} \\ &= Z_{c,r} - \psi_{c,r+1} + \delta_{c,r+1} \text{ (c.f. Equation 5)} \end{aligned}$$

Using the induction hypothesis, we have:

$$\begin{aligned} Z_{c,r+1} &= \left(\sum_{k=0}^{r} \delta_{c,k} + \delta_{c,r+1} \right) - \left(\sum_{k=0}^{r} \psi_{c,k} + \psi_{c,r+1} \right) \\ &= \sum_{k=0}^{r+1} \delta_{c,k} - \sum_{k=0}^{r+1} \psi_{c,k} \end{aligned}$$

Thus the relation holds for $r+1$.
Conclusion: Since Theorem 3.1 is verified for a null radius, and since assuming that it holds for a radius r allows deducing it also holds for $r+1$, we get that Theorem 3.1 is verified for any radius $r \in \mathbb{Z}^+$. □

This theorem is very useful in order to speed up the computation time of the detection, since it only requires to compute the two quantities $\delta_{c,r}$ and $\psi_{c,r}$ for all points $c \in \Omega$ and radii $R_{\min} < r < R_{\max}$. Actually, these quantities can easily be computed in a forward processing of the orientation map. If we consider a given orientation γ, we can build two structuring elements:

$$B_\gamma = \left\{ (d, r) \in \mathbb{Z}^2 \times \mathbb{Z}^+ / (K_{d,\tilde{0}^\gamma,r} = 1) \wedge (K_{d,\tilde{0}^\gamma,r-1} = 0) \right\}$$

and:

$$\overline{B}_\gamma = \left\{ (d, r) \in \mathbb{Z}^2 \times \mathbb{Z}^+ / (K_{d,\tilde{0}^\gamma,r} = 0) \wedge (K_{d,\tilde{0}^\gamma,r-1} = 1) \right\}$$

with $\tilde{0}^\gamma$ the point of Ω equal to $(0,0)$ whose orientation is γ.

These structuring elements allow us, for various points q of orientation γ, to list the corresponding centers c and the radii r that have to be considered during the computation of $\delta_{c,r}$ and $\psi_{c,r}$, respectively. Thus, if we pre-compute these structuring elements for various quantized orientations, we can choose for each pixel q the structuring elements whose orientation is the closer from the one of q and then, for each couple (d, r) update the values of $\delta_{q+d,r}$, and $\psi_{q+d,r}$, respectively, by increasing their value by 1. Doing this is just a way to propagate the impact of q to all centers that consider q as pointing toward them according to its orientation.

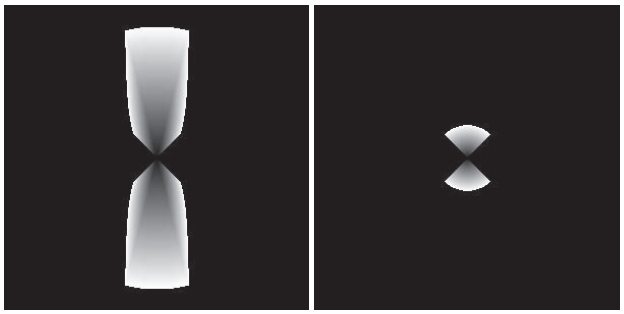

(a) (b)

Fig. 2. Example of B_γ (a) and $\overline{B_\gamma}$ (b) for a vertical orientation, $R_{\max} = 130$ and $\alpha = 0.25$. Gray levels represent the radius associated to each pixel offset. Offsets with a null radius do not belong to the structuring element.

Theorem 3.2. *$\forall d \in \mathbb{Z}^2, \forall \gamma \in [0, 2\pi[$, there exists at most one $r \in \mathbb{Z}^+$ such that $(d, r) \in B_\gamma$ and at most one $r' \in \mathbb{Z}^+$ such that $(d, r') \in \overline{B_\gamma}$.*

Proof. Due to the definition of $K_{c,q,r}$, for a given (c, q), either $K_{c,q,r} = 0$ for any r, or when r increases, $K_{c,q,r}$ goes from 0 to 1 and from 1 to 0 only one time. □

Figures 2(a) and 2(b) illustrate B_γ and $\overline{B_\gamma}$, respectively, for a vertical orientation. Because of Theorem 3.2, they can be both represented using a grayscale image where gray levels represent the radius associated the corresponding offset.

Additionally, let us mention that the detection of large lesions can be addressed using a multiscale approach allowing reducing $R_{\max}$ and the size of the structuring elements.

4. COMPLEXITY

We now focus on the complexity of the proposed approach in order to compare it to the straightforward implementation of Equation 1.

First for each pixel q of a slice, we need to process the points in B_γ and $\overline{B_\gamma}$ in order to compute $\delta_{c,r}$ and $\psi_{c,r}$, respectively. Using Theorem 3.2 and because B_γ is symmetric as shown in Figure 3(a), the number of elements in B_γ is given by:

$$\begin{aligned} |B_\gamma| = \; & 4 \left(\int_0^{\frac{\alpha R_{\max}}{\sqrt{\alpha^2+1}}} \sqrt{R_{\max}^2 - x^2}\,dx - \int_0^{\alpha R_{\max}\cos\left(\frac{\pi}{4}\right)} x\,dx \right. \\ & \left. - \int_{\alpha R_{\max}\cos\left(\frac{\pi}{4}\right)}^{\frac{\alpha R_{\max}}{\sqrt{\alpha^2+1}}} \sqrt{\frac{x^4}{(\alpha R_{\max})^2 - x^2}}\,dx \right) \\ \simeq \; & O(R^2) \end{aligned} \tag{6}$$

where the first term corresponds to the selection of points c that can reach the center of the structuring element in the worst case, which is the largest possible lesion (see non white areas in Figure 3(a)). The second and third terms aim at discarding points c that the center q of the structuring element cannot reach either because q would be in the hole of the ring centered at c or because a too large radius would be required in order to verify the convergence relation. They are represented by the two darkest zones in Figure 3(a).

The number of elements in $\overline{B_\gamma}$ is given by:

$$\begin{aligned} |\overline{B_\gamma}| \; & = 4 \left(\int_0^{\frac{\alpha R_{\max}}{\sqrt{2}}} \sqrt{\alpha R_{\max} - x^2}\,dx - \int_0^{\frac{\alpha R_{\max}}{\sqrt{2}}} x\,dx \right) \\ & = \frac{\pi \alpha^2 R_{\max}^2}{2} \\ & \simeq O(R^2) \end{aligned}$$

The two terms are illustrated in Figure 3(b).

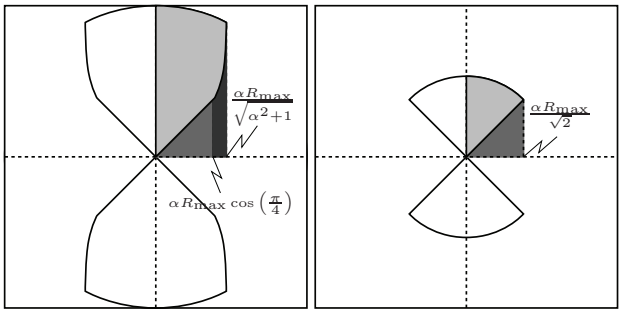

(a) (b)

Fig. 3. (a) Computation of $|B_\gamma|$ for a vertical orientation: the light gray area corresponds to $\frac{|B_\gamma|}{4}$ while the darkest areas correspond to second and third terms of Equation 6. (b) Same representation for $|\overline{B_\gamma}|$.

This results in a complexity of $O(NR_{\max}^2)$, with N the number of pixels in the image. In the case of a straightforward implementation of Equation 1, for each pixel we need to consider $R_{\max}$ ring-shaped neighborhoods resulting in the following amount of operations:

$$N \sum_{r=R_{\min}}^{R_{\max}} \pi r^2 - \pi(\alpha r)^2$$

leading to a complexity of $O(NR_{\max}^3)$.

Finally, we can discuss the impact of the constant α. In the case of the basic implementation, when it is close to 0, the surface of the ring to use becomes larger, while in the case of the proposed approach, the opposite behavior is observed: both $|B_\gamma|$ and $|\overline{B_\gamma}|$ decrease.

5. RESULTS

The approach was evaluated on a database containing 38 breasts reconstructed using the SART algorithm [5]. Ten of them were containing a biopsy-proven spiculated lesion or an architectural distortion. The remaining cases were used to evaluate the false positive fraction.

Because spiculated lesions and architectural distortions are not the only structures that respond to a convergence pattern (e.g. crossing or fibers), a last stage aiming at keeping only structures of interest was used. This step relies on the analyze of structure orientations found in the neighborhood of areas marked by the a contrario detector [2]. This time, orientations are not extracted from non correlated

gradient maps, but rather from Gaussian second derivatives of the slices along three directions. This is motivated by two reasons. First such an approach is more robust to noise, and second, combining these three filtered images allows us to obtain the exact orientation of structures under each pixel [1, 6]. The neighborhoods used in this step are deduced from the pairs (c, r) retrieved from the a contrario detection stage. The disks of radius r and centered at c associated to these pairs are aggregated leading to a binary set. The connected components of this binary set represent the neighborhoods to be used for the analysis of orientations. The key idea behind this analysis is that in the neighborhood of crossing of fibers, there are usually two or three fibers. This leads to one orientation per fiber resulting in two or three privileged orientations. In such a case, the histogram of orientations will have two or three peaks. Conversely, lesions usually radiate in all directions leading to an almost flat histogram. In order to distinguish between the two cases, the entropy of the histogram is used. Thus high values of this entropy will characterize spiculated lesions or architectural distortions, while low entropy values will correspond to false alarms. This step enables to decrease the number of false positives per case, which is a major concern for clinical use.

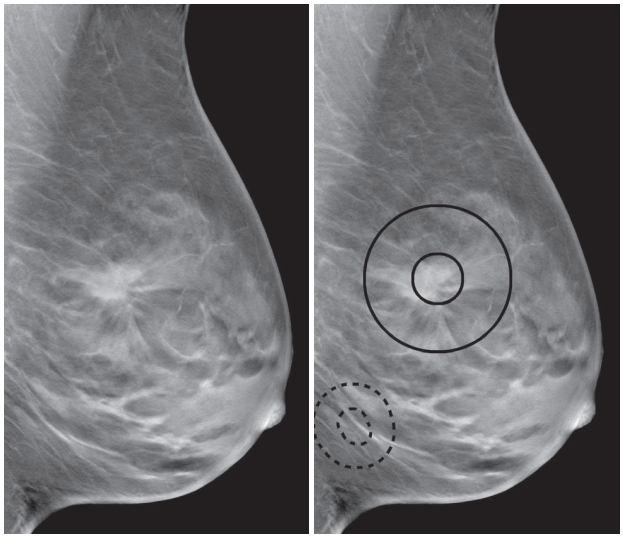

(a) (b)

Fig. 4. (a) A slice of a DBT volume containing a lesion. (b) Result after false positives reduction. A successfully removed false positive is marked in dotted lines.

Using the 38 breasts database, a sensitivity of 0.8 for 1.68 false positive per case was obtained, which is comparable to existing CAD systems for Digital Breast Tomosynthesis [7, 8, 9, 10]. This sensitivity was evaluated using the leave-one-out approach on the ten malignant cases: the detection for each lesion was evaluated using a threshold on the orientations entropy computed from the nine remaining cases. The threshold obtained using all malignant cases together was used to assess the false positive fraction on the remaining benign cases. Although no definite conclusion can be drawn due to the limited size of the database, this evaluation tends to validate the approach.

Figure 4 illustrates the detection result on a slice of a volume containing a spiculated lesion after false positive reduction.

6. CONCLUSIONS

In this paper we have addressed the problem of detection of convergence areas in an image. This work was motivated by the detection of spiculated lesions and architectural distortions in DBT datasets, which are suitably modeled by convergence patterns. In [2], a method based on an a contrario modeling was proposed in order to achieve this goal. Nonetheless, this approach is computationally intensive and may not be directly applied to process real data. For this reason, we have proposed a fast implementation. Our approach relies on two key features. First, the convergence index used during the detection is decomposed into two independent quantities using dynamic programming. Second, we proposed a way to efficiently compute these quantities using two families of structuring elements, which depend on the orientation of structures represented by each pixel in the image. The complexity of the obtained algorithm is $O(NR^2)$ compared to $O(NR^3)$ for the previous approach, which, associated to a multiscale approach, is suitable to process a DBT volume.

7. REFERENCES

[1] N. Karssemeijer and G. M. te Brake, "Detection of stellate distortions in mammograms," *IEEE Transactions on Medical Imaging*, vol. 5, no. 5, pp. 611–619, 1996.

[2] G. Palma, S. Muller, I. Bloch, and R. Iordache, "Detection of Convergence Areas in Digital Breast Tomosynthesis using a Contrario Modeling," in *SPIE Symposium on Medical Imaging*, Lake Buena Vista, FL, USA, feb 2009.

[3] A. Desolneux, L. Moisan, and J. Morel, "Meaningful alignments," *International Journal of Computer Vision*, vol. 40, no. 1, pp. 7–23, 2000.

[4] B. Grosjean, S. Muller, and H. Souchay, "Lesion detection using an a-contrario detector in simulated digital mammograms," 2006, vol. 6146, p. 61460S, SPIE.

[5] A. H. Andersen and A. C. Kak, "Simultaneous algebraic reconstruction technique (SART): A superior implementation of the ART algorithm," *Ultrasonic Imaging*, vol. 6, no. 1, pp. 81–94, 1984.

[6] J. J. Koenderink and A. J. van Doorn, "Generic neighborhood operators," *IEEE Trans. Pattern Anal. Mach. Intell.*, vol. 14, no. 6, pp. 597–605, 1992.

[7] H. D. Cheng, X. J. Shi, R. Min, L. M. Hu, X. P. Cai, and H. N. Du, "Approaches for automated detection and classification of masses in mammograms," *Pattern Recogn.*, vol. 39, no. 4, pp. 646–668, 2006.

[8] H. Chan, J. Wei, B. Sahiner, E. A. Rafferty, T. Wu, M. A. Roubidoux, R. H. Moore, D. B. Kopans, L. M. Hadjiiski, and M. A. Helvie, "Computer-aided Detection System for Breast Masses on Digital Tomosynthesis Mammograms: Preliminary Experience," *Radiology*, vol. 237, no. 3, pp. 1075–1080, 2005.

[9] H. Chan, J. Wei, Y. Zhang, M. A. Helvie, R. H. Moore, B. Sahiner, L. Hadjiiski, and D. B. Kopans, "Computer-aided detection of masses in digital tomosynthesis mammography: Comparison of three approaches," *Medical Physics*, vol. 35, no. 9, pp. 4087–4095, 2008.

[10] S. Singh, G. D. Tourassi, J. A. Baker, E. Samei, and J. Y. Lo, "Automated breast mass detection in 3D reconstructed tomosynthesis volumes: A featureless approach," *Medical Physics*, vol. 35, no. 8, pp. 3626–3636, 2008.